University of Groningen

Bachelor Project

The effect of the Peierls barrier on a discrete dislocation plasticity model for BCC iron

Author:
Thije Tjebbes *(s4137043)*

Supervisors:
Prof. dr. E. van der Giessen
dr. F. Maresca

Abstract

An existing 2D discrete dislocation plasticity (DDP) model of BCC iron is enhanced by adding the Peierls barrier. The model is fitted to an experimental stress-strain curve of BCC iron based on the method presented by Katiyar and Van der Giessen in [1]. It was found that using this fitting procedure it is possible to create a realistic representation of BCC iron with the addition of the Peierls barrier. However, the addition of the Peierls barrier did have some implications on the predictions. Both the dislocation as the obstacle density were increased to acquire the desired stress-strain curve. The dislocation density was compared to experimental data as well, which showed that the dislocation density at larger strain values, for 0.4% strain and more, matches the experimental data better for an increased Peierls barrier.

July 10, 2023

Contents

1 Introduction

The motion of dislocations in the crystal structure of metals describe how they behave under applied strain. While a lot of research is done into dislocation dynamics for thin films and face-centered cubic (FCC) crystals, the research into body-centered cubic (BCC) crystals is limited. However, this crystal structure is one of the most common structures found in metals, and is thus of great interest.

To comprehend the behaviour of the dislocations within the metal and understand how this affects the way the metal strains under applied stress, computational models are created. In traditional continuum plasticity models the dislocations are averaged out and only the essential characteristics of the plasticity are described. This overlooks the fact that several features of deformation on the micron/sub-micron scale are affected by single dislocations. Because of this, discrete dislocation plasticity (DDP) models were created. In these models the dislocations are seen as discrete entities while the crystal lattice is still described as a continuum. These models provide us with a lot of information about microplasticity within crystal structures. However, due to the complex structure of the dislocation loops and the interactions with the crystal the computational burden is enormous. therefore a 3D to 2D procedure is created to heavily reduce the weight of the calculations. These models have been extensively used over the past 20 years in research to dislocation physics. Although it does not capture all the details a 3D model is able to, it has been successfully used in research on microplasticity problems.

The 2D-DDP framework is widely used for FCC crystals, however the application to BCC crystals is more complicated. Katiyar and Van der Giessen [1] created a model that uses 2D-DDP framework for these BCC crystals. The difficulty for BCC crystals compared to FCC crystals is that the screw and edge dislocations have a different mobility compared to the equal mobility for FCC dislocations. In 2D-DDP all dislocations are seen as edge dislocations, this means an effective mobility that approximates a combination of the screw and edge dislocation is needed to represent the difference between them. This model was fitted to experimental data of BCC iron and was found to provide a good prediction when it was applied for different strain rates.

The 2D-DDP model has demonstrated a realistic approximation of the behaviour of dislocations in BCC iron. However, it does not take into account that a certain amount of stress is needed to bring a dislocation into motion when it is stationary, this is called the Peierls barrier τ_p. This research aims to enhance the existing model by incorporating the Peierls Barrier and investigating the influence on the model's accuracy. To achieve this, experimental data of the metal was used to see if the modified model can still be used to reproduce similar or more realistic results. By adding the Peierls barrier, an attempt was made to enhance the models realism and determine if this still yields a desirable outcome.

Section 2 starts with brief overview of dislocation physics, to provide the basic principles used in the 2D-DDP model. Using this, there will be a detailed examination of the model itself in section 3. The Peierls barrier will be described in section 4, and the way the model is initiated will be shown in section 5. Using this, section 6 will show the results from the simulations. Sections 7 and 8 will discuss these findings and conclude if the addition of the Peierls barrier is successful.

2 Dislocation plasticity

Metals are made from crystal structures that consist of repetitive lattice elements, such as the FCC and the BCC structure. The material is built up from multiple grains, which are differently oriented crystals divided by grain boundaries. In nature, these crystals contain defects that interfere with the perfect structure. These defects can range from zero to three dimensional. The emphasis in this research lies on the one dimensional defects: the so-called dislocations [2]. In figure 1 a dislocation loop is shown with its two main features, the tangent vector, $\hat{\mathbf{t}}$, that is tangent to the curve of the dislocation loop and varies along the loop and the Burgers vector, $\mathbf{b}$, that describes the lattice mismatch above and below the dislocation and is given by the magnitude and direction of the dislocation. Dislocations occur along slip planes, which are the closed packed planes in the crystal.

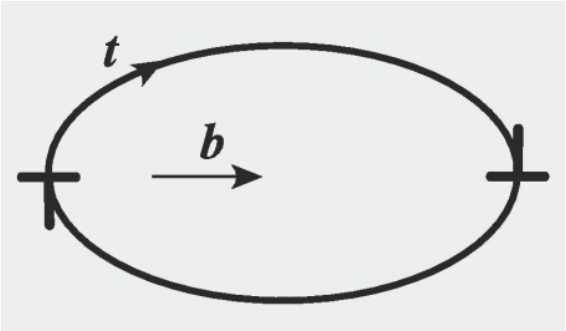

Figure 1: Simple illustration of a dislocation loop on a slip plane, with the Burgers vector $\mathbf{b}$ and the tangent vector $\mathbf{t}$ [1].

The behaviour of dislocations depends on the relation between $\hat{\mathbf{t}}$ and $\mathbf{b}$. If $\hat{\mathbf{t}}$ and $\mathbf{b}$ are perpendicular to each other it is called an edge dislocation. This can be visualized as an extra plain inserted into the crystal, with the dislocation at the tip of this extra plain. If $\hat{\mathbf{t}}$ and $\mathbf{b}$ are parallel it is called a screw dislocation, which can be visualised as cutting a crystal along a lattice plane and then sliding one side one atom upwards with respect to the other side. If the angle between $\hat{\mathbf{t}}$ and $\mathbf{b}$ is anywhere between these two options the dislocations are called mixed dislocations [3].

When stress is applied on the metal, dislocations can glide along the slip planes. Dislocations can be signed positive or negative, which influences the direction in which they glide. Positive dislocations glide in the same direction of the upper half of the shear stress, while negative dislocations glide in the opposite direction. The dislocations can be stopped by an obstacle on the slip plane or by grain boundaries. The movement of dislocations is called dislocation mobility, which is an important parameter for the behaviour of a crystal under stress, because it controls the plastic deformation, or plastic flow, within the crystal. Because of this, it regulates the rate of deformation [1].

To describe how the stress in the material relates to the effective force that is acting on the dislocation loop, the Peach-Koehler equation can be used, which is given by [4]

$$\mathbf{F} = (\boldsymbol{\sigma} \cdot \mathbf{b}) \times \hat{\mathbf{t}}, \tag{1}$$

where $\mathbf{F}$ is the force per unit length that acts on the dislocation loop, $\boldsymbol{\sigma}$ is the stress state at the point of the loop. Using the mobility of a dislocation loop, the Peach-Koehler force can also be used to determine the glide velocity of the loop [1],

$$v^{LP} = M(\theta) F_n, \tag{2}$$

where $M(\theta)$ is the mobility of the loop in the glide plane, and is a function of the angle θ between $\hat{\mathbf{t}}$ and $\mathbf{b}$. F_n is the magnitude of the Peach-Koehler force in the direction of the slip plane, that can be calculated by taking the length of the force vector $\mathbf{F}$ in the direction of the slip plane.

The plastic strain on the material can be described using the area A that is swept by the dislocation loop [5],

$$\boldsymbol{\varepsilon} = \sum \frac{A}{2V}(\mathbf{n} \otimes \mathbf{b} + \mathbf{b} \otimes \mathbf{n}), \tag{3}$$

Where $\mathbf{n}$ is the unit normal vector to the slip plane and V is the volume of the cell. Equation (2) and equation (3) can be used to calculate the plastic strain rate, when the velocity of the loop is integrated to calculate the rate of change of A [1],

$$\dot{\boldsymbol{\varepsilon}} = \frac{1}{2V} \oint v^{LP} dl (\mathbf{n} \otimes \mathbf{b} + \mathbf{b} \otimes \mathbf{n}). \tag{4}$$

Dislocations can be multiplied by so-called Frank-Read sources. Figure 2 shows the mechanism of the formation of dislocation loops from a Frank-Read source. A dislocation is pinned at its ends by two obstacles, as shown in panel 1 of figure 2. Due to an applied shear stress τ on the crystal, the dislocation will glide in the perpendicular direction to the line with a velocity v^{LP}. Panels 2 and 3 show how the dislocation gradually bows out due to the stress. When the dislocation expands beyond the half circular shape, it spontaneously expands further and spirals around the pinned points, as can be seen in panels 4 to 6. The stress needed to surpass this critical shape is given by [6]

$$\tau = \beta \frac{\mu b}{l_{FR}}, \text{ with } \beta = \frac{A}{2\pi}\left(\ln \frac{l_{FR}}{r_0} + B\right), \tag{5}$$

where μ is the shear modulus, l_{FR} is the length of the pinned dislocation, A displays the difference between screw and edge dislocations ($A = 1$ for screw dislocations and $A = 1/(1-\nu)$ for edge dislocations). B is associated with the dislocation core and r_0 is the core radius of the full dislocation [7]. When the dislocation is bowed out as far as in panel 5, the two ends of the semi circle meet and in turn annihilate to form a dislocation loop. After this, the pinned segment reforms and returns to the first state after which it starts forming another loop, as can be seen in panels 7 and 8 [3]. The time it takes for such a dislocation loop to form is the nucleation time t_{nuc}.

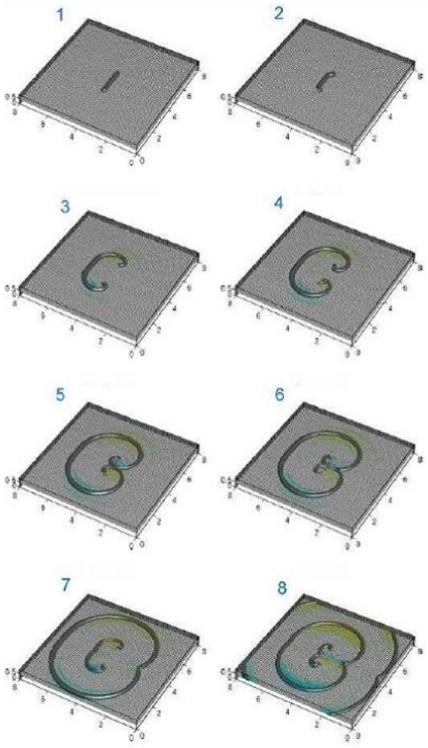

Figure 2: Snapshot from a numerical simulation of a Frank-Read source in a FCC crystal [3].

3 The 2D-DDP model

In the introduction, it was described that the 2D-DDP model is used for the simulation of the metal under applied strain because it gives a realistic approximation using a more time-efficient method compared to the 3D-DDP models. Both models make use of short range interactions, in which the dislocations are seen as discrete entities, and long range interactions, in which the crystal lattice is described as a continuum. In the 2D-DDP model the short range interactions are described using a set of rules that govern the motion of the discrete dislocations, the nucleation, the annihilation and the interaction with obstacles. The dislocation structure and stress state in the model are known at any given instance. The model computes the deformation, the stress state and the new configuration of dislocation for small time steps. When loading is applied the model is updated for each step. Each time step can be split into three computational stages. Firstly, the Peach-Koehler force needs to be determined for all dislocations. Secondly, the dislocation landscape needs to be determined by looking at the motion, the generation, the annihilation and the pinning of dislocations. Lastly, the stress and strain state for the new configuration of dislocations needs to be computed.

Dislocation loops are 2 dimensional in 3D, which means they need to be changed to an 1 dimensional projection in 2D. This results in a dislocation dipole consisting of two edge dislocations, which is illustrated in figure 3. The sign of the magnitude of the Burgers vector reflects the direction of the line. Using this simplification, the displacement discontinuity is contained on the line as it is within the loop in 3D.

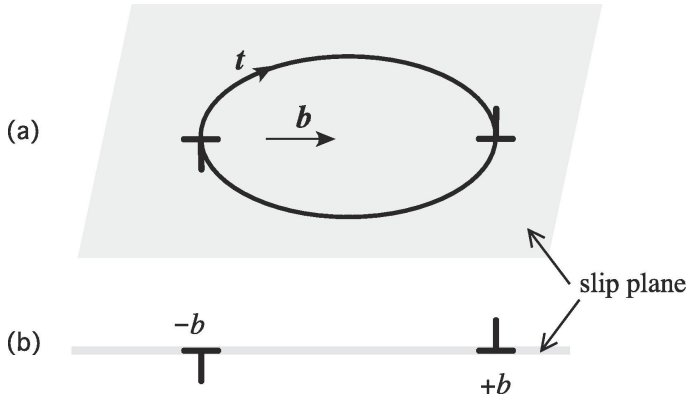

Figure 3: A 3D dislocation loop on a slip plane becomes an edge dislocation dipole in 2D with the same Burgers vectors [1].

In the materials of interest, pinned dislocations are present on the slip planes as obstacles for other dislocations. They are randomly distributed over the slip planes, with density ρ_{obs}. The obstacles are dimensionless and are only described by their strength. When a dislocation runs into such an obstacle, a pile up of dislocations can occur, which gives rise to large stresses in the area around the obstacle. When the stress on the pinned dislocation surpasses the obstacle strength τ_{obs}, the dislocation is released and is free to move.

The set of rules that describe the movement of the dislocations are designed to be simple, while preserving the essential physics [8]. The velocity of a dislocation is given by

$$v^{(i)} = \frac{F^{(i)}}{B}, \tag{6}$$

where $F^{(i)}$ is the Peach-Koehler force on that dislocation and B is the drag coefficient. Furthermore, annihilation occurs when two dislocations with Burgers vectors with opposite signs come within the material dependant annihilation distance, which is around a few times the Burgers vector.

Next to the short range interactions, that describe how the dislocations move, the long range interactions are governed by linear elastic fields that are computed using Boundary value problems (BVPs), which incorporates the boundary conditions imposed on the material. Real crystals are anisotropic, which means that the relationship between stress and strain is dependent on the orientation of the crystal [9]. When a polycrystalline framework is used, with different orientations for every independent crystal, elastic anisotropy needs to be included. Hooke's law can be used to describe linear elastic behaviour and is given by [8]

$$\sigma_{ij} = C_{ijkl}\varepsilon_{kl}, \tag{7}$$

where C_{ijkl} is the four-dimensional stiffness tensor. If we take the base vectors to align with the cube axes of the anistropic crystals we remain with the following non-zero elements of C_{ijkl} to describe the tensor: $C_{iiii} = C_{11}$, $C_{iijj} = C_{12}$ and $C_{ijij} = C_{44}$, where i and j range from 1 to 3 and $i \neq j$. Since plastic deformation is governed by the motion of dislocations, plastic anistropy is governed by the motion of dislocations on discrete slip systems [8].

3.1 Implementation of Frank-Read sources

In 3D, Frank-Read sources are created naturally when a dislocation is pinned at its ends. However, in 2D the source nucleates two dipoles instead of a loop, which leads to the point source being the right replacement, as is shown in figure 4. The Peach-Koehler force determines if the source generates a dislocation dipole, which occurs when the force exceeds $b\tau_{\text{nuc}}$, where τ_{nuc} is based on equation (5), for at least the nucleation time t_{nuc}. The sign of the dipole is dependent on the direction of the Peach-Koehler force.

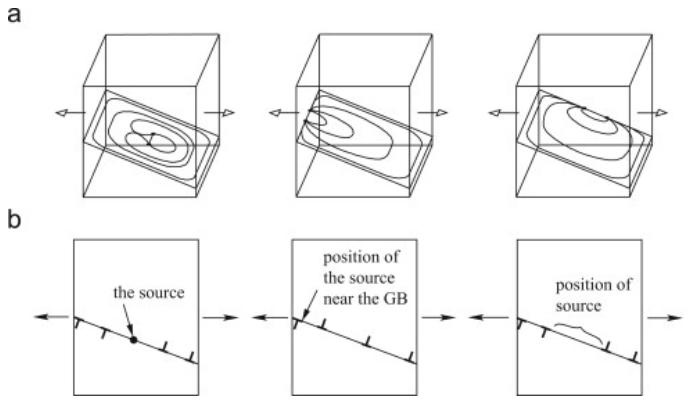

Figure 4: Schematic representation of a Frank-Read source in a grain in 3D (a) and the projection to 2D (b) [6].

In addition, the simplification to a point source has the implication that l_{FR} does not exist in 2D. Because l_{FR} is an important parameter to compute τ_{nuc}, as was shown in equation (5), values of it need to be generated in another way. Shishvan and Van der Giessen [6] assumed that l_{FR} follows a log-normal distribution of lengths, using equation (5) it can be shown that $1/\tau_{\text{nuc}}$ follows the same distribution which is also described fairly well by a log-normal distribution, as shown in figure 5. In a log-normal distribution very large values of l_{FR} are possible, while in reality l_{FR} is bounded by the grain size. Because of this, a maximum value of l_{FR} is introduced. However, the limiting values of τ_{nuc} are more interesting from a physical point of view, so $\tau_{\text{nuc}}^{\max}$ is designed based on its physical properties. The minimum stress can be calculated using equation (5), and is dependent on $l_{FR}^{\max}$. The maximum value is based on the theoretical shear strength of the material, τ_{th}, which is related to the shear modulus. For example, $\tau_{th} = \mu/18$ for Cu.

To change the value τ_{nuc} within the model, it is important to understand how $\tau_{\text{nuc}}^{\max}$ effects the distribution. In a log-normal function 99.7% of the area is located in the region $m \pm 3s$, where m

is the mean and s is the standard deviation. Because of the log-normal distribution we need to take the natural logarithm of τ_{nuc}, this yields:

$$\begin{cases} m - 3s = \ln \tau_{\text{nuc}}^{\max}, \\ m + 3s = \ln \tau_{\text{nuc}}^{\max}. \end{cases} \tag{8}$$

By changing the values of the minimum and the maximum stress, the mean value of the stress can be altered within the model.

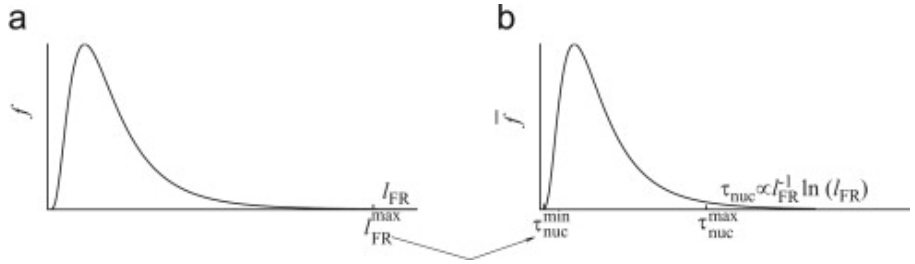

Figure 5: (a) Log-normal distribution of the source length l_{FR}, (b) which translates to a log-normal distribution for the strength τ_{nuc} [6].

The log-normal distribution on its own is not sufficient to describe τ_{nuc}, because material dependent obstacles around a source can be of influence on the Frank-Read mechanism. Such obstacles would increase the source strength, which can be modelled as follows, [6]

$$\tau_{\text{nuc}} = \tau_{\text{nuc}}^{LN} + \tau_{\text{nuc}}^{0}, \tag{9}$$

where τ_{nuc}^{0} represents the influence of these obstacles. This parameter is a material specific parameter that is found by fitting the data to experimental data.

The sources are implemented at the start of the simulation at a certain density, ρ_{nuc}. When the number of sources is too small, the influence of the outliers can become significant, which is not desirable. Because of this, a sufficiently large density of sources is needed to ensure the right distribution.

3.2 Modelling the BCC crystal structure

For a BCC crystal, figure 6 shows that there are 12 effective slip systems in 3D that translate to three effective slip systems in 2D. These are the slip systems on which the dislocation dipoles are allowed to move. The FCC crystal also renders three effective slip systems in 2D, that have a different orientation compared to BCC.

The major difference between the two structures is the difference in mobility of the dislocations. In FCC crystals, the mobility of edge and screw segments are equal, while in BCC crystals the screw segments are considerably slower than the edge segments. This means that the calculation of the effective mobility, which is a combination of the mobility of edge and screw dislocations, in 2D is more difficult to compute for BCC crystals. The 3D to 2D representation of the mobility can be seen in figure 7, which is based on equating the plastic strain rate of a dislocation loop in 3D to the plastic strain rate of a dislocation dipole in 2D.

To calculate the plastic strain rate of a dislocation loop in 3D, a shear stress τ is applied. Equation (1) can be used to describe the Peach-Koehler force as $F_n = \tau b$. Using equations (4) with $\mathbf{n}$ and $\mathbf{b}$ for a dislocation loop as shown in figure 7a, the following relation for the strain rate of a dislocation loop under applied shear stress can be derived [1],

$$\dot{\varepsilon}_{xy}^{LP} = \frac{b}{2V} \oint v^{LP} dl = \frac{b^2}{2V} \sigma_{xy} \oint M(\theta) dl, \tag{10}$$

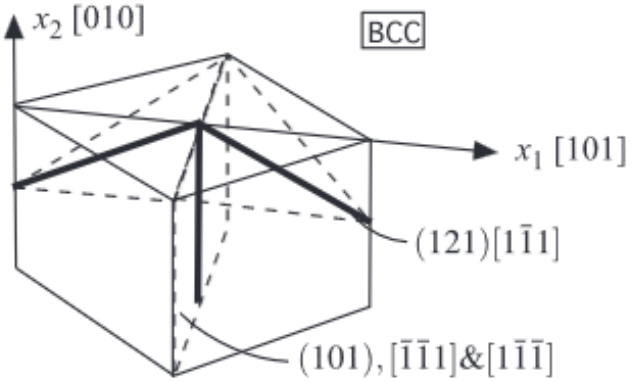

Figure 6: Effective slip systems in 2D (thick lines) and in 3D (dashed lines) on which plain strain plastic deformation is allowed [1].

where V is the volume in which the loop expands. $M(\theta)$ gives the mobility of any dislocation segment in terms of the edge and screw mobilities M_e and M_s and is given by

$$M(\theta) = \left(M_e^2 \sin^2\theta + M_s^2 \cos^2\theta\right)^{1/2}. \tag{11}$$

The plastic strain rate of the dislocation dipole in 2D, as shown in figure 7b, gives the following strain rate [1],

$$\dot{\varepsilon}_{xy}^{DP} = \frac{Lb^2 M_{\text{eff}} \tau}{V}, \tag{12}$$

where L is an out-of-plane length used to relate the relate the dipole to the loop and is given by

$$L = \frac{\pi D^2}{4s}, \tag{13}$$

with D the diameter of the dislocation loop and s the distance between the two edge dislocations within the dipole.

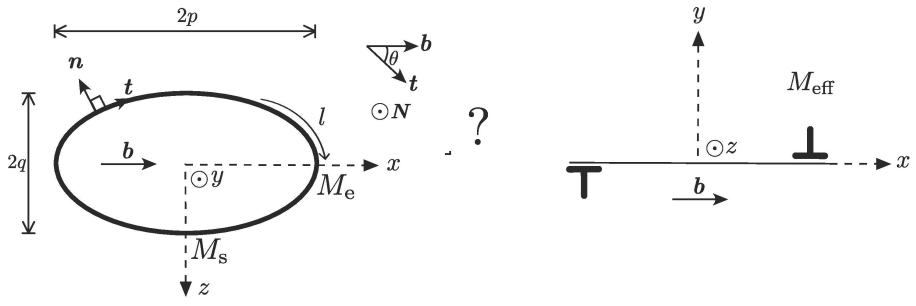

Figure 7: (a) Elliptical dislocation loop with the major axis $2p$ and the minor axis $2q$, **b** the burgers vector and **t** and **n** the unit line and unit normal vector. M_e and M_s are the mobilities of pure screw and edge segments. (b) The same situation translated to the edge dislocation dipole, with an as of yet unknown effective mobility M_{eff} [1].

Now, by imposing that the plastic strain rates are the same in both 2D and 3D, the densities for the dislocation loop and dipole can be equated, using equations (10), (12) and (11). It has been shown in [1] that M_{eff} can then be calculated to be

$$M_{\text{eff}} = M_s E\left[1 - \frac{M_e^2}{M_s^2 \alpha^2}\right] / E\left[1 - \frac{1}{\alpha^2}\right], \text{ with } E[k] = \int_0^{\pi/2} \sqrt{1 - k\sin^2\theta}\, d\theta, \tag{14}$$

where $\alpha = p/q$ is the aspect ratio of the loop. For α-iron $M_e = 10000$ Pa^{-1}s^{-1} and M_s is 100 Pa^{-1}s^{-1}. An aspect ratio of 1 describes a circular loop and gives a value for M_{eff} that is considerably lower than M_e, because of the influence of M_s. Figure 8 shows that M_{eff} becomes more screw like with an increasing aspect ratio. The maximum aspect ratio $\alpha_{\max}$ is given by M_e/M_s, which is 100 for α-iron. The aspect ratio can have values between 1 and $\alpha_{\max}$. Because it would be an enormous computational burden to keep track of the aspect ratio for every dislocation dipole, the mean value for M_{eff} is taken over the possible range of values for α. Figure 8 shows that the mean effective mobility can be calculated to be $\langle M_{\text{eff}} \rangle = 475$ Pa^{-1}s^{-1}.

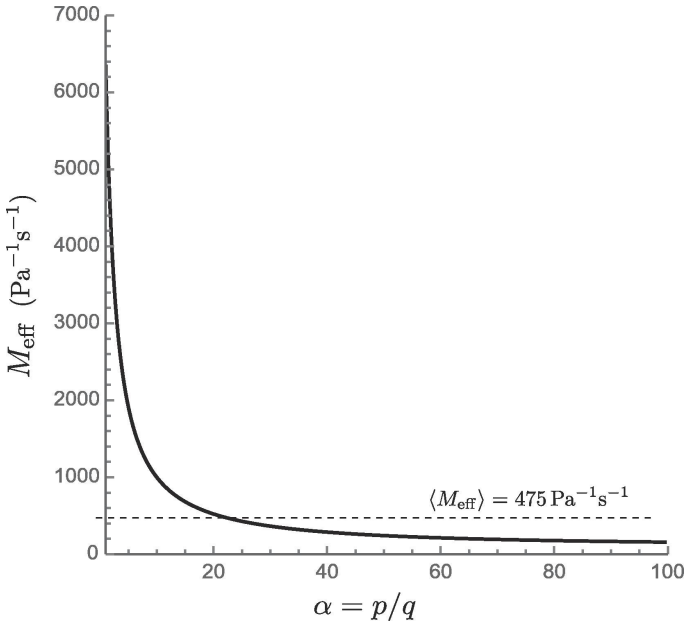

Figure 8: The effective mobility for an increasing aspect ratio for α-iron, the computed mean effective mobility is shown with a dashed line [1].

4 The Peierls barrier

For dislocations to be able to move, a certain amount of stress needs to be applied on the crystal. This is because the energy of the dislocation is at a minimum when it is stationary in a position that is favorable parallel to its glide plane. When a dislocation is moved out of this position, the configuration of atoms is altered, which increases the energy of the configuration. This energy is called the Peierls barrier and to move the dislocation over this barrier a certain amount of shear stress in the direction of **b** is needed, called the Peierls stress τ_p. The height of the Peierls barrier is dependent on the structure in which the dislocation is present [10] and also on whether the dislocation is a screw or an edge dislocation. The equation for the Peierls stress is given for screw and edge dislocations respectively by [11]:

$$\tau_p^s = G \exp\left(\frac{4\pi\zeta}{b}\right), \text{ with } \zeta = \frac{d}{2}, \tag{15}$$

$$\tau_p^e = \frac{G}{1-\nu} \exp\left(\frac{4\pi\zeta}{b}\right), \text{ with } \zeta = \frac{d}{2(1-\nu)}. \tag{16}$$

In these equations G is the shear modulus, ν is the Poisson's ratio and d is the interspacing between slip planes.

The expressions (15) and (16) reveal that, like the mobilities, the Peierls barriers for edge and screw segments differ. A similar method as with the mobility can be used to calculate the effective Peierls stress τ_p^{eff} along the dislocation loop, using equation (11),

$$\tau_p(\theta) = \left((\tau_p^e)^2 \sin^2\theta + (\tau_p^s)^2 \cos^2\theta\right)^{1/2}. \tag{17}$$

With this equation and with equation (14), where τ_p^s and τ_p^e are used instead of M_s and M_e, and $\alpha = 1$, because the dislocation loop is circular at the initiation of the loop expansion, τ_p^{eff} is given by

$$\tau_p^{\text{eff}} = \tau_s E \left[1 - \frac{\tau_e^2}{\tau_s^2}\right]. \tag{18}$$

The effective Peierls stress is calculated using the Peierls barrier for both edge and screw segments at absolute zero, because these values are computed in previous research. The barrier for the edge segment is given as 0.536 GPa [12] and the barrier for screw segments is gives as 2.025 GPa [13], a numerical approximation of (18) computes to $\tau_p^{\text{eff}} \approx 1.391$ GPa.

4.1 Integration of the Peierls barrier in the 2D-DDP model

Before any simulations are done, it is important to know how an increasing barrier affects the model. The Peierls barrier was added in the existing model for different values of τ_p to see the influence on both the yield stress σ_y, which is the amount of stress needed to go from the elastic to the plastic regime, and the strain hardening rate, which is the amount of stress needed to strain the material in the plastic regime. Figure 9a shows the stress-strain curve for five values of τ_p ranging from 0 MPa to 1391 MPa. In figure 9b the 0.2% yield stress values are plotted against the Peierls barrier. This shows a linear relation between the Peierls barrier and the yield stress. In figure 9a the effect of τ_p on the strain hardening rate can be seen for τ_p ranging from 0 MPa to 500 MPa, which shows a decrease of strain hardening for an increasing Peierls barrier to the point of strain softening, which means that decreasing stress is needed for further strain.

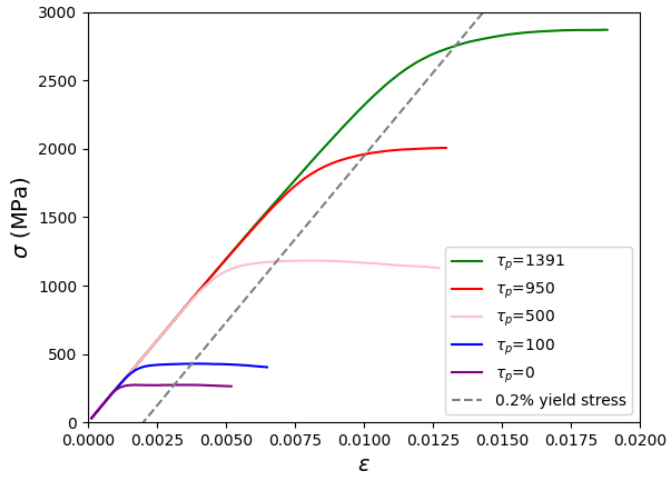

(a)

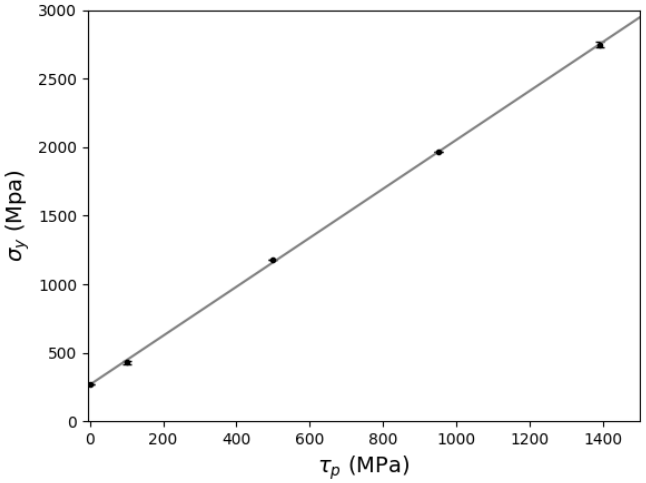

(b)

Figure 9: (a) The stress-strain curve of BCC Iron for different values of the Peierls stress (τ_p). (b) The relation between the yield stress and the Peierls stress for BCC Iron.

The main implication of a higher yield stress is that more dislocations are created during the elastic regime, but that they do not yet move significantly. Figure 10 shows that the density of dislocations in the model ρ_{dis} increases with increasing strain for all values of τ_p. Furthermore, it

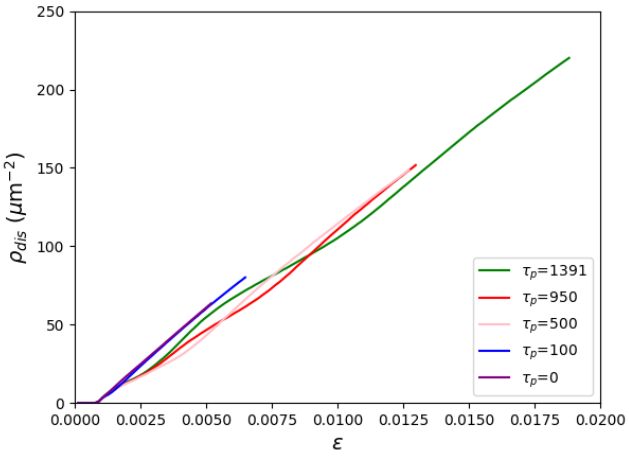

Figure 10: Predicted dislocation density ρ_{dis} for increasing strain for different values of the Peierls stress (τ_p).

also takes more time steps to reach the plastic regime in these cases. Because of these two reasons the time it takes to compute the stress-strain curve using $\tau_p = 1391$ MPa is significantly longer than for $\tau_p = 100$ MPa.

Figure 9a shows that the influence of τ_p on both the yield stress and the strain hardening rate is already significant for a value of 100 MPa. Taking this and the fact that the computational burden using $\tau_p = 1391$ MPa is increased heavily into consideration, calculations will from now on be made using $\tau_p = 100$ MPa.

5 Setup of the model

As mentioned in the introduction, this research is a continuation of the research of Katiyar and Van der Giessen in 2010 [1]. The research created a 2D-DDP model for BCC iron that was fitted to a high strain rate, and used to predict lower strain rates. The results were in fairly good agreement with the experimental data. In this paper an addition was made to the model by including the Peierls barrier. The goal of this research is to find the impact of this addition by comparing the DDP model with and without the Peierls barrier. By fitting the unknown parameters of the redesigned DDP model, using the same setup, a new fit will be created to check if the model is still able to generate a realistic outcome.

5.1 Problem formulation

In single crystals the calculations for anisotropic elasticity and plasticity are relatively straight forward [8]. However, the 2D-DDP model is applied to a polycrystalline material, consisting of multiple grains with impenetrable grain boundaries. In such a system, the elastic properties are not homogeneous, due to the different orientations of each crystal. Shishvan et al. [8] show that by using a superposition framework this can be accounted for. The BVP for this system can now be decomposed into two problems. Firstly, all grains are treated as separate crystals and become a set of DD sub-problems that are treated using 'generic' boundary conditions. Secondly, the whole body is treated as a fully elastic sub-problem that is subject to the global boundary conditions. Once both are solved, the solution of the actual BVP can be written as the superposition of the two sub-problems.

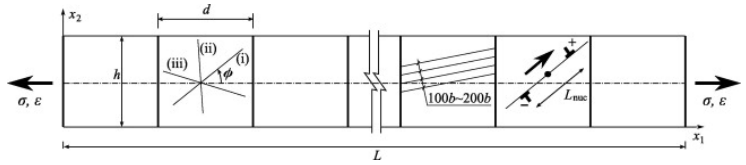

Figure 11: Array of grains in a thin film, with grain size d and thickness h. Slip systems, slip planes and a source are indicated from left to right [8].

To model polycrystalline iron, a framework can be set up using a 2-dimensional array of rectangular grains, based on the thin film seen in figure 11. It shows how multiple grains with size d, are placed next to each other. Each grain has three slip directions in the same ratio with respect to each other, but each shifted with a distinct angle ϕ with respect to the grain. ϕ Is chosen randomly for all grains with a uniform distribution. Parallel planes in the grain are spaced with a distance of $200b$. The grain boundaries are impenetrable for dislocations, while they are able to freely leave the top and bottom. Frank-Read sources are implemented on the slip planes as point sources at a density ρ_{nuc}, with the source strength τ_{nuc} given by equation (9). Furthermore, obstacles are added on the slip planes at a density of ρ_{obs} and with a strength τ_{obs}.

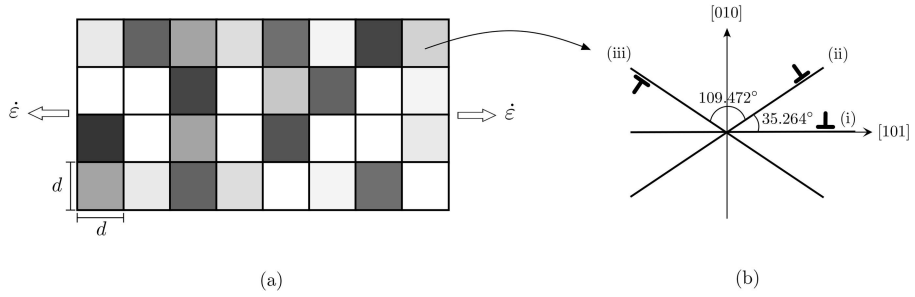

Figure 12: (a) A 2-dimensional array of square grains with grain size d, exposed to an uniaxial strain rate. (b) Each grain has the same three effective slip systems unique to the BCC crystal under plane strain, but these are differently oriented with respect to the x-axis [1].

To model BCC iron the thin film model is used with multiple layers as can be seen in figure 12. A 4 x 8 framework is chosen with all boundaries impenetrable, including the top and bottom. The tensile strain rate is imposed at the ends, while the top and bottom are assumed to be traction free. The four layers are based on previous DDP studies that showed the free surface effect reduces heavily for three or more layers. The eight grains per layer are chosen to give a statistically meaningful tensile response. The grain size in BCC iron is ∼45 µm. However, it is chosen as 10 µm in the model, because for a smaller grain size the Hall-Petch effect starts dominating, while a larger grain size becomes too computationally heavy [1]. The Hall-Petch effect is the fact that for increasingly small grain sizes the strain hardening rate increases as well as the yield stress [14]. Figure 13 shows that for low and high source densities the Hall-Petch effect dominates at smaller grain sizes and vanishes for a grain size of 10 µm.

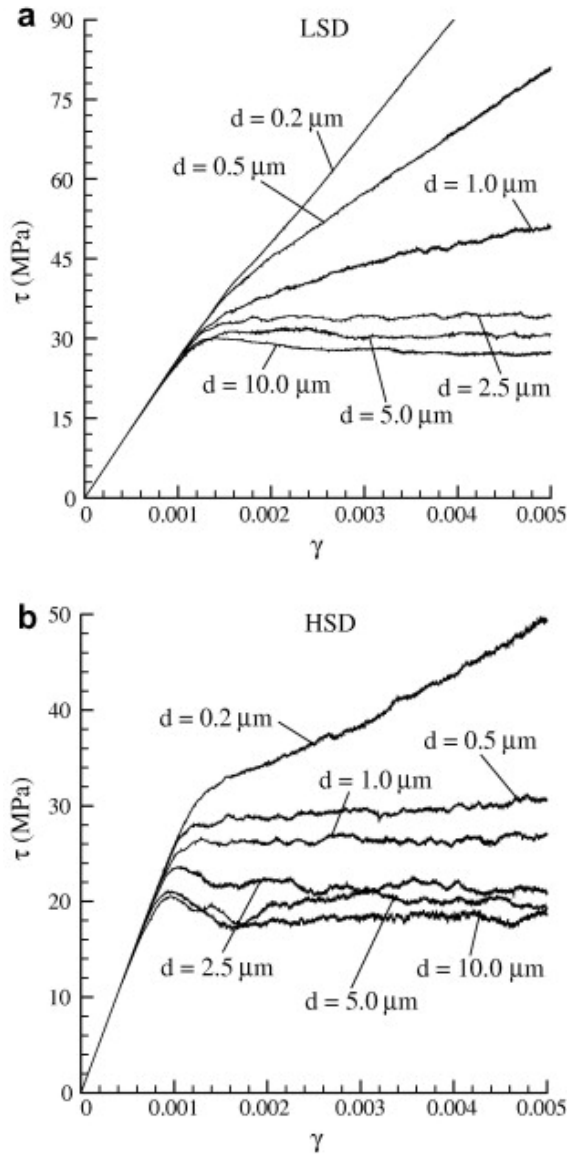

Figure 13: Hall-Petch effect on the stress strain curve of iron for (a) low source densities and for (b) high source densities for a combination of FCC and BCC grains. [14].

The strain rate used in the measurements is based on the experimental data found by Weston [15]. The strain rates in this paper vary from 10^{-3} to 10^{4}, as can be seen in figure 14. The flow stress at different strain rates differs significantly. At low strain rates the flow stress increases slowly, which can be attributed to the fact that the flow stress is driven by thermal activation. At higher strain rates, the flow stress is limited by the mobility of dislocations and increases more rapidly. Because the DDP model is driven by the mobility of dislocations and not by thermal activation, simulations will only be valid at higher strain rates. Furthermore, a high strain rate has a lower computational burden. For these reasons, the highest strain rate seen in figure 14, $\dot{\varepsilon} = 5200$ s^{-1}, is used to for the simulations.

For single crystalline iron the Burgers vector is $b = 0.25$ nm, and the elastic constants are $C_{11} = 229$ GPa, $C_{12} = 134$ GPa and $C_{44} = 115$ GPa. Due to the small number of grains the Young's Modulus is slightly adjusted with respect to the experimental value to $E = 210$ GPa [1]. The experimental yield strength σ_y used for the fitting procedure is found to be ~ 330 MPa. The experimental hardening rate at a strain rate of 5200 s^{-1} is found to be ~ 10000 MPa [1].

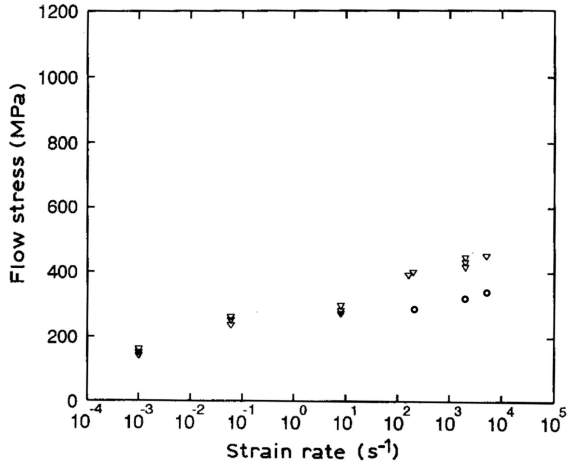

Figure 14: The peak stress values at different strain rates of Iron, indicated with '$\triangledown$' [15], with the 0.2% yield stress values indicated with '$\circ$' [1].

5.2 Fitting parameters

Having chosen $\tau_p = 100$, four unknown parameters are left that can be used to fit the stress-strain curve to the experimental values. The fitting parameters are the source density ρ_{nuc}, the source strength τ_{nuc}, the obstacle density ρ_{obs} and the obstacle strength τ_{obs}. The source strength is chosen using the fact that the resolved shear stress scales linearly with the tensile stress:

$$C = \frac{\tau_{\text{nuc}} + \tau_p}{\sigma_y} = \frac{237 + 0}{270} = \frac{\tau_{\text{nuc}} + 100}{430},$$

where τ_p is added to τ_{nuc} to reflect the resolved shear stress with and without the barrier and the yield stress is taken from the approximation in figure 9. Since C represents that this division remains constant, τ_{nuc} can be calculated to be 277 MPa. The other parameters will be initiated based on the results found by Katiyar and Van der Giessen [1]. The obstacle strength was found to be $\tau_{\text{obs}} = 7\ \tau_{\text{nuc}}$. To ensure a realistic log-normal distribution of strengths, the nucleation density ρ_{nuc} was chosen as 20 µm^{-2}. The obstacle density was found to be $\rho_{\text{obs}} = 7\ \rho_{\text{nuc}}$.

From this starting point the obstacle density and strength will be varied to obtain the experimental hardening rate. After this, the nucleation strength will be adjusted to find the experimental yield strength.

6 Results

Using the initial conditions, the green curve in figure 15a was found. It can be clearly seen that the strain hardening rate does not match the desired strain hardening rate, which is shown as the dotted grey line. To fit the desired strain hardening rate, first $\tau_{\text{obs}}/\tau_{\text{nuc}}$ was varied. When this was found to be insufficient, $\rho_{\text{obs}}/\rho_{\text{nuc}}$ was increased and the measurements were repeated. By further increasing $\tau_{\text{obs}}/\tau_{\text{nuc}}$ to 11 the wanted strain hardening rate was obtained, which can be seen as the pink curve in figure 15.

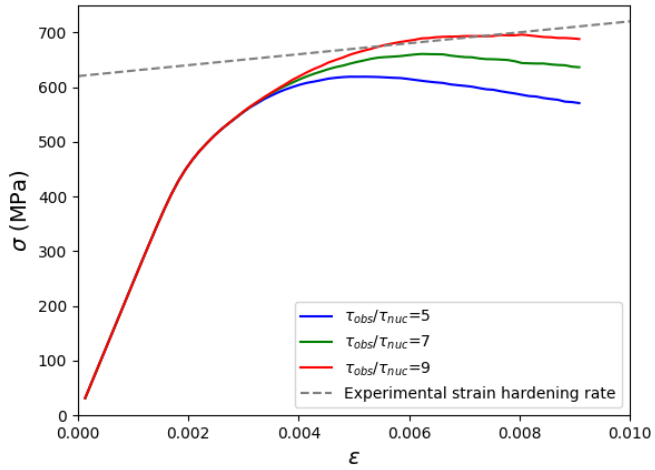

(a) $\rho_{\text{obs}}/\rho_{\text{nuc}} = 7$

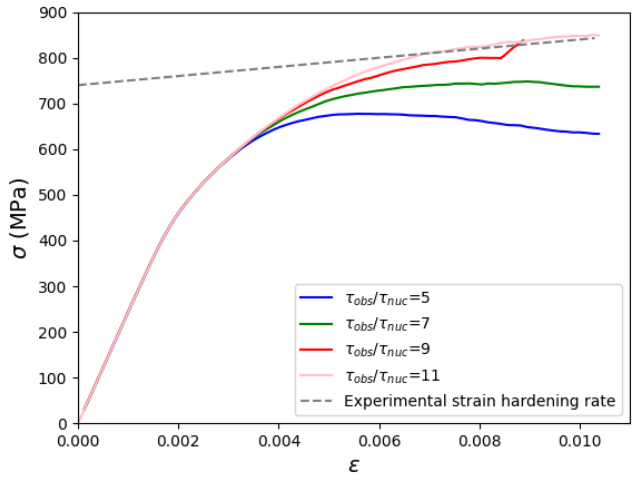

(b) $\rho_{\text{obs}}/\rho_{\text{nuc}} = 9$

Figure 15: Stress-strain curves for $\tau_{\text{obs}}/\tau_{\text{nuc}} = 5$, 7, 9 and 11 and $\rho_{\text{obs}}/\rho_{\text{nuc}} = 7$ and 9. The experimental strain hardening rate is plotted for comparison.

However for this result, the yield stress was found to be 735 MPa. Since the experimental value is ∼330 MPa, τ_{nuc} needs to be lowered significantly. To do this both τ_{nuc}^{LN} and τ_{nuc}^{0} in equation (9) need to be lowered. The log-normal component was lowered by adjusting the upper boundary of the distribution, which gave a mean value of 57 MPa. By adjusting the value of τ_{nuc}^{0} the results of figure 16 are obtained.

The red curve in figure 16 corresponds to a yield stress of 401 MPa. This means that to obtain the wanted yield stress τ_{nuc} needs to be dramatically lowered. It also shows that the strain

hardening rate dropped completely, which means that $\tau_{\text{obs}}/\tau_{\text{nuc}}$ as well as $\rho_{\text{obs}}/\rho_{\text{nuc}}$ need to be increased further in order to achieve a good match with the experimental data.

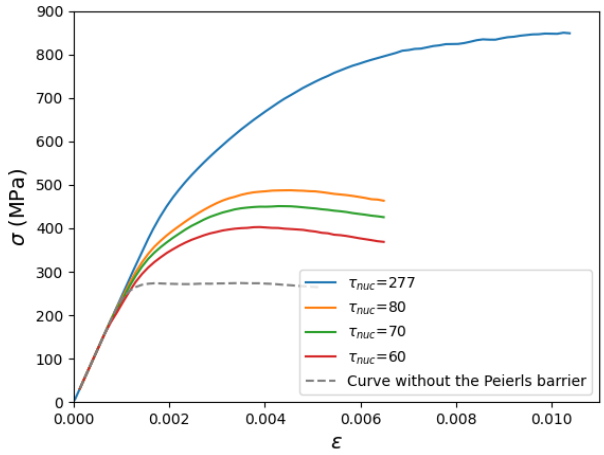

Figure 16: Stress-strain curves for decreasing values of the average nucleation stress (τ_{nuc}).

Figure 10 shows that the impact of the Peierls barrier itself on the rate of change of the dislocation density is negligible. However, both $\tau_{\text{obs}}/\tau_{\text{nuc}}$ and $\rho_{\text{obs}}/\rho_{\text{nuc}}$ are increased to obtain a good fit to the experimental stress-strain curve for an increasing Peierls barrier. This yields a different dislocation landscape within the model compared to simulations without these adjustments. The rate of change of the dislocation density increases due to this change in the dislocation landscape, as shown in figure 17. In this figure, $\tau_{\text{obs}}/\tau_{\text{nuc}} = 11$ and $\rho_{\text{obs}}/\rho_{\text{nuc}} = 9$ are used for $\tau_p = 100$ MPa and $\tau_{\text{obs}}/\tau_{\text{nuc}} = 7$ and $\rho_{\text{obs}}/\rho_{\text{nuc}} = 7$ for $\tau_p = 0$ MPa. These values might be increased even further for the simulations with the Peierls barrier, when we keep in mind that the strain hardening rate in figure 16 dropped.

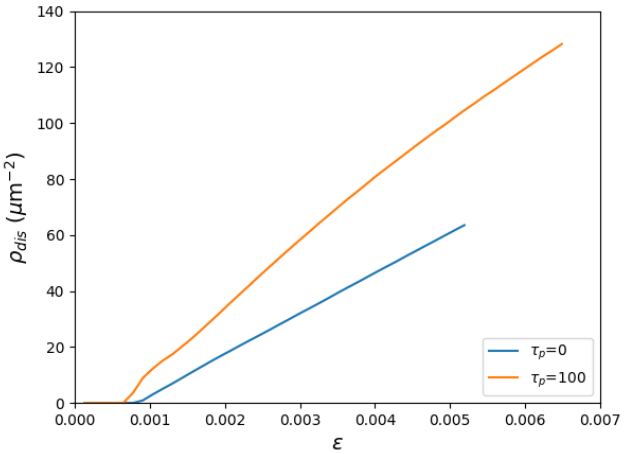

Figure 17: Dislocation density (ρ_{dis}) for increasing strain, for the model with and without the addition of the Peierls barrier.

To put figure 17 into perspective we can compare it with the dislocation density found at different strain rates for iron, which is shown in figure 18. From this figure and figure 17, table 1 is created to compare the dislocation density at 0.4% to 0.6% strain.

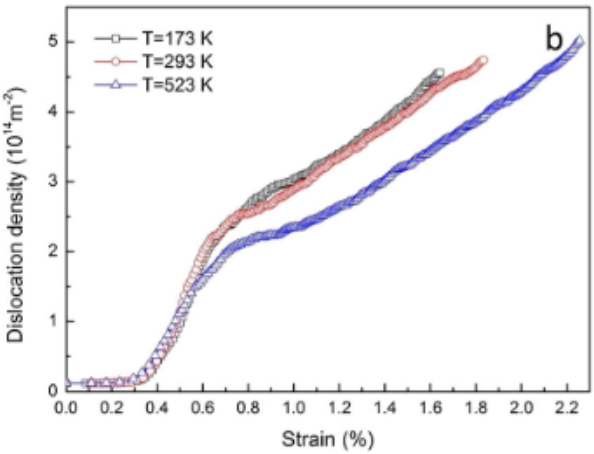

Figure 18: Dislocation density for increasing strain for Iron at different temperatures [16].

strain (%)	ρ_{dis} for $\tau_p = 0$	ρ_{dis} for $\tau_p = 100$	experimentally found ρ_{dis}
0.4	50	85	40
0.5	60	105	100
0.6	70	120	200

Table 1: Dislocation densities (μm^{-2}) for simulations with and without the Peierls barrier compared to experimental data.

7 Discussion

The results found by fitting the parameters to the experimental data do not yet yield a sufficient fit to the experimental data. The method that is used can be repeated until the right fit is found. However, the method that was used by Katiyar and Van der Giessen in [1] did not work as expected. The main problem was that when the nucleation stress was lowered, the strain hardening rate also dropped, while this was not the case without the Peierls barrier. The reason for this might be that the nucleation stress was lowered more heavily with the Peierls barrier than without. This also influences the obstacle strength, since $\tau_{\text{obs}} = 11\ \tau_{\text{nuc}}$. By lowering the obstacle strength, obstacles are unpinned more frequently and dislocations are more mobile. This can result in strain softening.

The results found in figure 15 are based on a single configuration of sources and obstacles in the model. Multiple realisations are needed to validate these results. The results for $\tau_p = 100$ MPa seen in figure 9b are based on multiple realisations. The mean of these results was taken and the result that came closest to this mean was used in further simulations. In this way, the configuration of sources and obstacles in the model that yields the most average results was used trough out the research. However, this is a blunt simplification, that has no real ground to stand on. To really validate the results, simply more realisations are needed.

The values found for τ_p^s and τ_p^e were expected to have a ratio of $\tau_p^e/\tau_p^s = 1.52$ when looking at equations (15) and (16), while the ratio between the values found in literature yield $\tau_p^e/\tau_p^s = 0.26$. This is a significant difference, while both of the values were found using pure BCC iron at 0K. It might be due to the fact that the interspacing between slip planes differs in the two situations, since the calculations of τ_p^s were done with approximately four times the amount of atoms between the slip planes compared to the calculations of τ_p^e. Incorporating this brings the ratio between τ_p^s and τ_p^e closer to the expected ratio. The effect of this would be that the value of τ_p^{eff} could be in the region between 0.4 GPa and 3.0 GPA. This region is much broader, but still remains above the value of 0.1 GPa, which is the value used for the fitting procedure. This means the conclusions about the results are still valid.

As can be seen in the results, $\tau_p = 100$ MPa was used to fit to the experimental data instead of the expected value of τ_p. This choice is simply due to the high computational burden with higher Peierls barriers. Figure 9 shows that both the yield stress and the strain hardening/softening are influenced by the addition of the Peierls barrier, as well as by an increasing Peierls barrier. Because the addition of the Peierls barrier is expected to already generate different results, the effect that this barrier has is already of interest. However, this means that the effects seen due to the addition of a lower Peierls barrier might need to be amplified to also create a realistic model for the theoretically found Peierls barrier. To validate this, some realisations of the model including the higher Peierls barriers could be used.

More realisations were halted because of in physical situations occurring during the simulation. The most common error was due to two equally signed dislocations colliding. When looking at the difference between the model with and without the barrier, it can be seen that more dislocations are present in the model with the barrier. Furthermore, the obstacle density is increased as well. This means that there are more dislocations that have a higher chance to form a pile-up. Since this error occurs mostly in regions where very high stresses are found between two dislocations of equal signs, and pile-up form the possibility for this, it makes sense that this error occurs more frequently in the model with the Peierls barrier.

The use of equation (17) gives an approximation of the effective Peierls barrier. However, it must be noted that this remains a simplification from 3D to 2D, which means that some of the important 3D mechanisms are ignored. Furthermore, the aspect ratio is simply taken to be one. This is validated by the fact that an initiated dislocation by a Frank-Read source will be circular. However, this is also a simplification that does not take any exceptions into consideration. The simplification towards 2D is needed to reduce the computational cost of the DDP model, but will always decrease its realism.

8 Conclusion

The stress-strain curve found for BCC iron using a Peierls barrier of $\tau_p = 100$ MPa did not yet yield a good approximation of the experimental stress-strain curve. However, By doing more iterations of the method used to fit the model to the data, it should be possible to get a good approximation.

The addition of the Peierls barrier resulted in an increased amount of dislocations and obstacles. When compared to experimental data about dislocation densities in iron, it shows that in the elastic regime the dislocations do not yet form for both the experimental data and the simulated results. However, the elastic regime for the experimental data lasts longer than in the simulations, for which the reason has not yet been found. For this reason, the comparison between the simulations and the experimental data is made in the region where the dislocation densities increases for both cases. When the rate of change of dislocation densities is compared for the model with and without the Peierls barrier, it can be seen that the simulations with the addition of the Peierls barrier yield a better approximation to the experimental data. By taking into consideration that a higher Peierls barrier might further increase the rate of change in dislocation density, the simulations with the addition of the effective Peierls barrier might approach the experimental rate.

The addition of the Peierls barrier also influences the transition from the elastic to the plastic regime in the stress-strain curve. The transition is less abrupt and follows a more rounded curve than the stress-strain curve without the Peierls barrier.

To conclude, the computational burden of the model is increased and simulations are more frequently stopped due to in physical behaviour within the model. However, the addition of the Peierls barrier increases the accuracy of dislocation densities at higher strain. More realisations and realisations with different Peierls barriers are needed to verify that the addition of the Peierls barrier enhances the model.

References

[1] T. Katiyar and E. van der Giessen. "Effective mobility of BCC dislocations in two-dimensional discrete dislocation plasticity". In: *Computational Materials Science* 187 (2021), p. 110129.

[2] W. Cai and W.D. Nix. *Imperfections in crystalline solids*. Cambridge University Press, 2016.

[3] C. Fressengeas. *Mechanics of dislocation fields*. John Wiley & Sons, 2017.

[4] V.A. Lubarda. "Dislocation Burgers vector and the Peach–Koehler force: a review". In: *Journal of Materials Research and Technology* 8.1 (2019), pp. 1550–1565.

[5] H. Fan et al. "Strain rate dependency of dislocation plasticity". In: *Nature communications* 12.1 (2021), p. 1845.

[6] S.S. Shishvan and E. van der Giessen. "Distribution of dislocation source length and the size dependent yield strength in freestanding thin films". In: *Journal of the Mechanics and Physics of Solids* 58.5 (2010), pp. 678–695.

[7] S. Xu et al. "An analysis of key characteristics of the Frank-Read source process in FCC metals". In: *Journal of the Mechanics and Physics of Solids* 96 (2016), pp. 460–476.

[8] S.S. Shishvan et al. "Plane-strain discrete dislocation plasticity incorporating anisotropic elasticity". In: *International Journal of Solids and Structures* 48.2 (2011), pp. 374–387.

[9] V. Maupin and J. Park. "1.09—Theory and observations—Seismic anisotropy". In: *Treatise on geophysics* 20 (2015), pp. 277–305.

[10] P. Guyot and J.E. Dorn. "A critical review of the Peierls mechanism". In: *Canadian Journal of Physics* 45.2 (1967), pp. 983–1016.

[11] J.N. Wang. "Prediction of Peierls stresses for different crystals". In: *Materials Science and Engineering: A* 206.2 (1996), pp. 259–269.

[12] R. Chang and L.J. Graham. "Edge dislocation core structure and the peierls barrier in body-centered cubic iron". In: *physica status solidi (b)* 18.1 (1966), pp. 99–103.

[13] F. Maresca et al. "Screw dislocation structure and mobility in body centered cubic Fe predicted by a Gaussian Approximation Potential". In: *npj Computational Materials* 4.1 (2018), p. 69.

[14] D.S. Balint et al. "Discrete dislocation plasticity analysis of the grain size dependence of the flow strength of polycrystals". In: *International Journal of Plasticity* 24.12 (2008), pp. 2149–2172.

[15] G.M. Weston. "Flow stress of shock-hardened Remco iron over strain rates from 0.001 to 9000 s- 1". In: *Journal of materials science letters* 11.20 (1992), pp. 1361–1363.

[16] W. Zhou et al. "Dislocation behavior in nickel and iron during laser shock-induced plastic deformation". In: *The International Journal of Advanced Manufacturing Technology* 108 (2020), pp. 1073–1083.